Soft Matter

Check for updates

Enhancing nanoscale viscoelasticity characterization in bimodal atomic force microscopy†

Casey Erin Adam,[a] Alba Rosa Piacenti,[a] Sarah L. Waters[b] and Sonia Contera [ID] *[a]

Polymeric, soft, and biological materials exhibit viscoelasticity, which is a time dependent mechanical response to deformation. Material viscoelasticity emerges from the movement of a material's constituent molecules at the nano- and microscale in response to applied deformation. Therefore, viscoelastic properties depend on the speed at which a material is deformed. Recent technological advances, especially in atomic force microscopy (AFM), have provided tools to measure and map material viscoelasticity with nanoscale resolution. However, to obtain additional information about the viscoelastic behavior of a material from such measurements, theoretical grounding during data analysis is required. For example, commercially available bimodal AFM imaging maps two different viscoelastic properties of a sample, the storage modulus, E', and loss tangent, $\tan\delta$, with each property being measured by a different resonance frequency of the AFM cantilever. While such techniques provide high resolution maps of E' and $\tan\delta$, the different measurement frequencies make it difficult to calculate key viscoelastic properties of the sample such as: the model of viscoelasticity that describes the sample, the loss modulus, E'', at either frequency, elasticity E, viscosity η, and characteristic response times τ. To overcome this difficulty, we present a new data analysis procedure derived from linear viscoelasticity theory. This procedure is applied and validated by performing amplitude modulation–frequency modulation (AM–FM) AFM, a commercially available bimodal imaging technique, on a styrene–butadiene rubber (SBR) with known mechanical behavior. The new analysis procedure correctly identified the type of viscoelasticity exhibited by the SBR and accurately calculated SBR E, η, and τ, providing a useful means of enhancing the amount of information gained about a sample's nanoscale viscoelastic properties from bimodal AFM measurements. Additionally, being derived from fundamental models of linear viscoelasticity, the procedure can be employed for any technique where different viscoelastic properties are measured at different and discrete frequencies with applied deformations in the linear viscoelastic regime of a sample.

1 Introduction

The mechanical properties of soft and polymeric materials underpin material function and application.[1,2] Most soft materials, from biological structures to rubbers, are considered to be viscoelastic, meaning they respond to externally applied deformations with time delays, τ, that emerge from a combination of both elastic (with elasticity E, Pa) and viscous (with dynamic viscosity η, Pa s) behavior.[1,2] Material properties E, η, and τ arise from nanoscale interactions between polymers and other molecules within the material when a stimulus is applied.[1,2] Each constituent molecule of the material, and each conformation of the constituent molecules, potentially contributes a unique E, η, and τ to the material's viscoelastic response across temporal and spatial scales.[1–6] Quantifying E, η, and τ of a material, especially at the nanoscale, provides insight into how polymers interact within a material, and how the material functions.[1–5]

Often, viscoelasticity is measured by dynamic experiments, which quantify the complex modulus E^* of a material.[1,2] E^* contains a storage component E', called the storage modulus, and a dissipative/loss component E'', called the loss modulus.[1,2] E' (Pa) measures the contribution of the sample's response that is in-phase with the applied stimulus, and represents energy stored by the sample per unit volume.[1,4,5,7] E'' (Pa) measures the out-of-phase component of the sample's response, and quantifies the energy per unit volume dissipated by the sample during

[a] Department of Physics, University of Oxford, Oxford, OX1 3PU, UK.
 E-mail: sonia.antoranzcontera@physics.ox.ac.uk
[b] Department of Applied Mathematics, Mathematical Institute, University of Oxford, OX2 6GG, UK

† Electronic supplementary information (ESI) available. See DOI: https://doi.org/10.1039/d4sm00671b

mechanical stimulus.[1,4,5,7] The ratio between both quantities, $\tan\delta = E''/E'$, is a measure of mechanical damping by the material.[7] Both E' and E'' are functions of material E and η, and τ, as well as the frequency at which the material is deformed.[1,2] The exact relation between E', E'', $\tan\delta$, and E, η, τ depends on a model of viscoelasticity specific to the material.[1,2]

One of the most widely used models of viscoelasticity is the General Maxwell Model (GMM).[1,5,6,8] The GMM assumes that a material exhibits linear viscoelasticity, where all E and η are constants independent of the applied stimulus.[1,5,8] As shown in Fig. S1 (ESI†), the GMM is often represented as a spring with elastic constant E_c connected in parallel with N arms that each consist of a spring with elastic constant E_n and damper with dynamic viscosity η_n connected in series.[1,5,8] Here, subscript n represents the nth arm of the material. Each arm has a unique relaxation timescale $\tau_n = \eta_n/E_n$ and creep timescale $\tau_c = \eta_n/E_c$.[1,5,8] Subscript c denotes that a spring contributes to the creep timescale. The simplest GMM contains $N = 1$ arms, thereby three material constants: E_c, E_r, and η, two timescales: $\tau_c = \eta/E_c$ and $\tau_r = \eta/E_r$, and is called the standard linear solid (SLS).[1,5,8] Since $N = 1$ for the SLS, the subscript r denotes that the spring in arm 1 is the only spring that contributes to the relaxation timescale of the SLS. The GMM is several SLSs connected in parallel.[1,8] Special cases of the SLS are the Maxwell (MW) and Kelvin–Voigt (KV) models.[1,8] For the MW model, $E_c \rightarrow 0$ and the material has two constants: E_r, and η.[4] MW materials have only one relaxation timescale, $\tau_r = \eta/E_r$.[1,5,8] For the KV model, $E_r \rightarrow \infty$ and the material has two constants: E_c, and η.[1,5,8] KV materials have only one creep timescale, $\tau_c = \eta/E_c$.[1,5,8] Experimentally, it is often not possible to measure all N arms of a GMM's response because N can be large, unless the material obeys the SLS, MW, or KV models.[9–13]

Often, the model to describe a sample's viscoelastic response, as well as the relevant material constants, are calculated from experimental measurements, and not measured directly.[1,2] For example, dynamic experiments, where an oscillatory stimulus is applied to a sample, are used to quantify E', E'', and $\tan\delta$, of a sample.[1,2] The model, and the relevant model parameters (E, η, τ) to describe the material's response are then determined from these dynamic quantities.[1,2] Several experimental techniques exist to perform dynamic measurements. One widely used technique for macroscale measurements is dynamic mechanical analysis (mDMA), which applies an oscillating axial or torsional stimulus to a sample.[2,14] For measurements at the nanoscale, atomic force microscopy (AFM) is a particularly useful tool because AFM can probe a sample with nanometer resolution, can be performed in liquid, does not require sample processing, and has higher resolution and more localized control than other techniques such as optical and magnetic tweezers.[15,16] Additionally, cutting edge developments in AFM allow more sophisticated dynamic measurements to be performed. For example, novel AFM developments use photothermal excitation of a cantilever to perform nanoscale dynamic mechanical analysis (nDMA) to measure E', E'', and $\tan\delta$ over a continuous range of frequencies that covers several orders of magnitude.[14,17] Additionally, bimodal imaging techniques such

as amplitude modulation–frequency modulation AFM (AM–FM AFM) exploit cantilever resonances to obtain high resolution quantitative maps (images) of a sample's nanoscale mechanical properties.[15,18–28] Bimodal imaging is particularly convenient because sample indentations are small, typically only a few nanometers,[19] allowing measurement of thinner samples, and increasing measurement spatial resolution.[19] Additionally due to the small indentations,[19] it is reasonable to assume that samples are measured in their linear viscoelastic regime.[5]

In bimodal AFM, the surface of a sample is intermittently tapped *via* a tip connected to a cantilever that is oscillated at two of the cantilever's eigenmodes.[18,19,25] At the lower frequency eigenmode, with frequency f_1 and angular frequency $\omega_1 = 2\pi f_1$, the cantilever has stiffness k_1, and the resonance peak at f_1 has quality factor Q_1.[18,19,25] The cantilever's vibration at the first mode has amplitude $A_{r,1}$ far from the sample, amplitude A_1 on the sample, and phase ϕ_1.[18,19,25] Similarly, the oscillation at the higher frequency eigenmode has frequency f_2, angular frequency $\omega_2 = 2\pi f_2$, stiffness k_2, quality factor Q_2, amplitude $A_{r,2}$ far from the sample, amplitude A_2 on the sample, and phase ϕ_2.[18,19,25] These properties of the cantilever (k, Q, f) and bimodal oscillation (A_r, A, ϕ) can be used to calculate viscoelastic properties of a sample as detailed in Section S4 (ESI†).[18,26–28] Briefly, each eigenmode is subjected to various types of feedback, depending on the bimodal imaging technique.[18] The lower eigenmode is typically subjected to amplitude modulation, which allows calculation of a sample's $\tan\delta_1$ (subscript 1 indicates that $\tan\delta$ is measured at f_1) from power dissipated and stored by the cantilever (see note S4.1, ESI†).[26,27] The higher eigenmode, with frequency f_2 and angular frequency $\omega_2 = 2\pi f_2$, is subjected to various types of modulation, and allows calculation of a sample's E'_2 (subscript 2 indicates that E' is measured at f_2) from the frequency shift of the second eigenmode caused by tip/sample interaction forces (details in Section S4.1, ESI†).[18,28] The most common form of bimodal AFM applies amplitude modulation to the first mode, frequency modulation to the second, and is referred to as amplitude modulation–frequency modulation AFM (AM–FM AFM).[18]

In order to calculate E'_2 in bimodal AFM, knowledge of the tip/sample interaction geometry is required.[18,28] In most cases, the Hertz contact model is applied.[18,28] The Hertz model assumes that both the indenter and sample are spherical, homogeneous, elastic materials, and that no adhesion is present between the indenter and sample.[5] Therefore, the calculated E'_2 can be incorrect for samples with an adhesive contact.[5] More details on the calculation of $\tan\delta_1$ and E'_2 are provided in Section S4.1 (ESI†). Additionally, the fact that E'_2 and $\tan\delta_1$ are characterized only at two discrete and different frequencies in bimodal imaging means that the full sample response remains unknown without additional data processing. Since bimodal AFM was developed to accurately quantify $\tan\delta_1$ and E'_2 from the cantilever's motion,[18,26–28] less emphasis has been placed on extracting additional information about the sample's viscoelastic response. This article describes how additional information about the viscoelastic behavior of a sample can be obtained from $\tan\delta_1$ and E'_2.

Bimodal AFM does not directly quantify a sample's loss modulus E'', nor material constants such as τ, E_c, E_r, and η. Quantification of E'' and material constants from bimodal AFM's $\tan \delta_1$ and E_2' is not straightforward because $\tan \delta$ and E'' depend on the frequency of the applied stimulus (per the formulas in Table S1, ESI†). Therefore, $\tan \delta_1$ and E_2' cannot be directly combined to calculate a sample's E'' and material constants. To circumvent this issue, it is typically assumed that the sample is a KV material, for which E' is independent of frequency.[24] Under this assumption, E'' and material constants E_c, η, and τ_c can be calculated from the measured $\tan \delta_1$ and E_2' as follows.[24] In the following equations, numbers in subscripts indicate the eigenmode to which the quantity corresponds.[24]

$$E_c = E_2' = E' \tag{1}$$

$$E_1'' = \tan \delta_1 E' \tag{2}$$

$$\eta = \frac{\tan \delta_1 E'}{\omega_1} \tag{3}$$

$$\tau_c = \frac{\eta}{E_c} \tag{4}$$

This approach has two main issues. First, assuming that the sample is a KV material may be incorrect, since the model of viscoelasticity that best applies to a sample is not immediately apparent[29] from E_2' and $\tan \delta_1$. Second, for samples that exhibit relaxation such as MW materials, SLSs, or GMMs, assuming that the sample is a KV material prevents quantification of the sample's relaxation time(s). Therefore, a new method of analyzing bimodal AFM data is needed.

This article describes the development and validation of a bimodal AFM data analysis procedure to extract additional information about sample viscoelasticity. This additional information includes the linear viscoelastic model that describes a sample and estimates of model parameters, which represent ensemble averages for the sample. The new analysis procedure first uses measured $\tan \delta_1$ and E_2' to determine the best model of linear viscoelasticity to describe a sample. Only models of linear viscoelasticity are considered in this analysis, due to the fact that bimodal AFM indentations are small,[19] and therefore likely in the linear viscoelastic regime of a sample. Once the model is determined from the model test, the sample's viscoelastic material constants are calculated from model test parameters. Finally, applying the selected model and calculated material constants allows reconstruction of the sample's $E'(f)$, $E''(f)$, and $\tan \delta(f)$. In this article, the analysis procedure is derived first, then validated on AM–FM AFM measurements of a styrene–butadiene rubber (SBR) with known viscoelastic properties.

This article also addresses another potential issue in bimodal AFM experiments in the calculation of E_2'. As detailed in Section S4.1 (ESI†), calculation of E_2' in bimodal AFM requires knowledge of tip geometry, in particular the tip radius, R.[18] Typically, R is determined via calibration on a sample of known

E_2'.[19] For this calibration, the user manually enters R in the software so the measured E_2' matches the expected E_2' of the calibration sample.[19] Calibration of R can also indicate whether the Hertz contact model on which bimodal AFM's calculation of E_2' is based,[18,28] is a good model for the tip/sample interaction.[19] When it is not possible to obtain the expected E_2' by calibrating R, it is a sign that the contact may be adhesive, and therefore that the Hertz model inadequately describes the contact geometry.[19]

In spite of the benefits of calibrating R, it is sometimes difficult to determine the best calibration sample for materials with multiple components. Additionally, calibration can damage or blunt the tip, changing R, before bimodal AFM is performed on the actual sample. Therefore, it would be convenient to skip calibration of R while still being able to correctly quantify material E_2'. The feasibility of doing so is assessed in this article.

2 Development of a novel analysis procedure for bimodal AFM data

It is not trivial to calculate the material constants of a sample (such as τ, E_c, E_r, and η) from bimodal AFM observables (E_2' and $\tan \delta_1$) because both E' and $\tan \delta$ are frequency dependent. To overcome this difficulty, a new bimodal AFM analysis procedure is derived in this section. The procedure uses the measured $\tan \delta_1$ and E_2' to determine which model of viscoelasticity a sample obeys (Section 2.1), calculate the relevant material constants of the sample (Section 2.2), and use these material constants to reconstruct $E'(f)$, $E''(f)$, and $\tan \delta(f)$ of the sample over a large frequency range (Section 2.3).

2.1 Determining the viscoelastic model that describes a sample

The first step in the new bimodal AFM data analysis procedure is to determine which model of viscoelasticity applies. It is reasonable to assume that samples exhibit linear viscoelasticity during a bimodal AFM experiment because sample deformations during bimodal imaging are small, typically only a few nanometers,[19] and are therefore likely in the sample's linear viscoelastic regime.[5] Therefore, only standard models of linear viscoelasticity: the MW, KV, SLS, and GMM are considered here.

A test to determine whether a sample is a MW, KV, or SLS material can be derived from the following expressions for E', E'', and $\tan \delta$ of the SLS.[1,5,8]

$$E' = E_c + \frac{E_r \eta^2 \omega^2}{E_r^2 + \eta^2 \omega^2} \tag{5}$$

$$E'' = \frac{E_r^2 \eta \omega}{E_r^2 + \eta^2 \omega^2} \tag{6}$$

$$\tan \delta = \frac{E''}{E'} = \frac{E_r^2 \eta \omega}{(E_c + E_r)\eta^2 \omega^2 + E_r^2 E_c} \tag{7}$$

Note that, for the SLS, E' is a function of E''.

$$E' = E_c + \tau_r \omega E'' \tag{8}$$

Eqn (7) can be rewritten in terms of $\tau_c = \eta/E_c$ and $\tau_r = \eta/E_r$ as follows.

$$\frac{1}{\tan \delta} = \frac{\omega}{\tau_c}\left[\tau_r^2 + \tau_r\tau_c + \frac{1}{\omega^2}\right] \tag{9}$$

The ratio of $\tan \delta$ measured at two different frequencies, such as the first and second eigenmode of the cantilever, can therefore be calculated as follows.

$$\frac{\tan \delta_2}{\tan \delta_1} = \frac{\omega_1}{\omega_2}\left[\frac{\tau_r^2 + \tau_r\tau_c + \frac{1}{\omega_1^2}}{\tau_r^2 + \tau_r\tau_c + \frac{1}{\omega_2^2}}\right] \tag{10}$$

Next, eqn (8) can be re-written in terms of $\tan \delta$ by dividing both sides of the equation by E' and rearranging terms.

$$\tan \delta = \frac{1}{\omega\tau_r}\left[1 - \frac{E_c}{E'}\right] \tag{11}$$

Bimodal AFM measures E' at the second eigenmode, so eqn (11) can be solved for $\tan \delta_2$, then substituted into eqn (10).

$$\frac{1}{\tan \delta_1} = \frac{E_c}{E'_2 \tan \delta_1} + \omega_1\tau_r\left[\frac{\tau_r^2 + \tau_r\tau_c + \frac{1}{\omega_1^2}}{\tau_r^2 + \tau_r\tau_c + \frac{1}{\omega_2^2}}\right] \tag{12}$$

Therefore, a plot of $y = \tan \delta_1^{-1}$ against $x = \left(E'_2 \tan \delta_1\right)^{-1}$ should be linear, with a slope $m = E_c$ and a y-intercept b dictated by material τ_r and τ_c, if the material is a SLS.

For a MW material, $E_c \approx 0$ and $\tau_c \to \infty$. Substituting these conditions into eqn (12) gives $m = 0$. Additionally, since $\tau_c \gg \tau_r$ and $\tau_c \gg \omega_{1 \text{ or } 2}^{-2}$, the intercept, b, can be approximated as follows.

$$b = \omega_1\tau_r \tag{13}$$

Therefore, eqn (12) simplifies to the following.

$$\frac{1}{\tan \delta_1} = \omega_1\tau_r \tag{14}$$

A graph of $y = \tan \delta_1^{-1}$ against $x = \left(E'_2 \tan \delta_1\right)^{-1}$ (eqn (12)) will be a horizontal straight line for a MW material.

For a KV material, $E_r \approx \infty$ and $\tau_r \approx 0$. Substituting these conditions into eqn (12), m is the same as that for the SLS, but $b = 0$. Eqn (12) simplifies to the following.

$$\frac{1}{\tan \delta_1} = \frac{E_c}{E'_2 \tan \delta_1} \tag{15}$$

The plot of $y = \tan \delta_1^{-1}$ against $x = \left(E'_2 \tan \delta_1\right)^{-1}$ will be a straight line through the origin for a KV material.

In summary, if a plot of bimodal AFM observables $\tan \delta_1^{-1}$ vs. $\left(E'_2 \tan \delta_1\right)^{-1}$ is linear, the sample can be modeled as a SLS, MW, or KV material. It remains unclear whether the plot will also be linear for a GMM, which will be assessed in the following section. Goodness of fit metrics, such as the R^2 value, for linear fits to bimodal AFM data can determine if one of these three models describes the sample. The slope and

y-intercept of the fit can then be used to distinguish between each model.

2.1.1 Extension to a GMM. The model test line (eqn (12)) could also work for a GMM, assuming it is possible to approximate the GMM as an SLS. Such an approximation is reasonable in certain cases, since the GMM consists of N SLSs connected in parallel, each with a unique elastic constant E_n, viscous constant η_n and time response τ_n (details in Section S1, ESI†).

For most GMM materials, the total number of arms in the GMM, N, is large. However, the distribution of the N different τ_n typically only has a few peaks, with values at different orders of magnitude (*i.e.* $\tau_n = $ ns, μs, ms, s, min, *etc*...).[9-13] Depending on the excitation stimulus, some peaks (subgroups) in the distribution of τ_n will contribute more to the sample's response than others. Arms that contribute most to the material's response to a dynamic stimulus of frequency f have τ_n on the order of $1/f$,[29] because arms with larger τ_n respond too slowly to contribute much to the material's response, and arms with faster τ_n only contribute briefly to the material's initial response to the stimulus, leaving arms with $\tau_n \approx 1/f$ to dominate the majority of the response. For example, a material's response to a dynamic stimulus with a frequency in the kHz range, like that applied by bimodal AFM, is more likely to be dominated by GMM arms with τ_n on the order of μs–ms.[29]

Assuming that bimodal AFM only excites one subgroup of GMM arms that have similar τ_n, the subgroup could be approximated as a single SLS, likely with a large standard deviation in E_c, E_r, and η due to the variety of arms contributing to this approximation. In other words, the model test line in eqn (12) could still be fitted to bimodal data from a GMM. However, because the governing equations of the GMM and SLS are different, the slope and y-intercept of the GMM model test line (eqn (12)) are not the same as that for the SLS, as follows.

While the line in eqn (12) could still be fit to bimodal measurements of a GMM, it is not possible to directly relate E_c or other material parameters to the slope, m_{GM}, and y-intercept, b_{GM}, of this line because there are too few AFM observables and too many unknowns, even if only a subgroup of GMM arms is excited. The unknowns include: E'_1, $\tan \delta_2$, E''_1, E''_2, E_c, the number of arms N (for the material as a whole or for the subgroup of arms), and the N different E_n and η_n. However, it is possible to use m_{GM} and b_{GM} to obtain bounds for the GMM's E_c, as detailed in Section S6 (ESI†). Briefly, algebraic manipulations (see Section S6, ESI†) of the expressions for E' and $\tan \delta$ of a GMM (Section S1 and Table S1, ESI†) result in the following expression.

$$\frac{E_c}{E'_2} < 1 - \tan \delta_1 b_{GM} - \frac{m_{GM}}{E'_2} + \frac{E_c}{E'_1} \tag{16}$$

Here, numbers in subscript indicate the eigenmode. The only unknowns in eqn (16) are E_c and E''_1. For a GMM (see formulas in Table S1, ESI†), $0 < E_c/E' \le 1$. These limits can be substituted into eqn (16) to obtain a more $\left(E_c/E'_1 = 0\right)$ or less $\left(E_c/E'_1 = 1\right)$ restrictive bound on E_c. Assuming that E_c is close to the bound on E_c allows the value of E_c to be approximated

from these bounds. The more restrictive bound results in eqn (17).

$$E_c \sim E_2'(1 - \tan\delta_1 b_{GM}) - m_{GM} \qquad (17)$$

The less restrictive bound results in eqn (18).

$$E_c \sim E_2'(2 - \tan\delta_1 b_{GM}) - m_{GM} \qquad (18)$$

Since the value of E_c is estimated by setting E_c equal to E_c's bound, the most restrictive estimate of the bound (eqn (17)) should be used when possible to avoid inadvertently over-estimating E_c. Should nonphysical, for example negative, values of E_c arise from applying eqn (17), then eqn (18) should be used instead. A detailed derivation and discussion of these points can be found in Section S6 (ESI†).

To estimate E_c of a GMM for this article, it is assumed that the value of E_c is approximately equal to this upper bound. Therefore, this method has the potential to overestimate the value of a GMM's E_c in samples where this assumption does not hold. Before applying this method, the reliability of calculating E_c via this assumption, and compared to treating the sample solely as a SLS must be assessed (see Table 1).

2.2 Solving for material constants from bimodal AFM data

Note that, if the sample is a KV material, all material constants (τ_c, η, E_c) can be calculated for each point in the bimodal AFM map via eqn (1)–(4). Therefore, the calculations in this section are to determine ensemble average material properties $(\tau_c, \tau_r, \eta, E_c, E_r)$ of MW, SLS, and GMM materials.

For materials obeying the GMM, there are too few knowns to calculate all material constants. Since only E_c (via eqn (12) for SLS or MW materials or via eqn (17) or (18) for GMM materials), $\tan\delta_1$ (via bimodal AFM measurements), and E_2' (via bimodal AFM measurements) are known, it is not possible to calculate the number of arms N in the material, nor all N values of E_n, η_n, and τ_n. Therefore, to estimate properties of a sample obeying the GMM, it is necessary to again assume that the subgroup of GMM arms contributing most to the sample's response can be approximated as a single SLS, likely with a large standard deviation in the values of E_r and η. Therefore, the following manipulations apply for all but KV materials.

As derived in the previous sections, $E_c = 0$ for MW materials. The slope and y-intercept of the model test line (eqn (12)) can be used to calculate E_c for the SLS and the upper bound of E_c (eqn (17) or (18)) for a GMM. The remaining material constants $(E_r, \eta, \tau_r = \eta/E_r$, and $\tau_c = \eta/E_c)$ can be determined from E_2', $\tan\delta_1$, and E_c via the expressions for E' and $\tan\delta$ of the SLS (eqn (5) and (7), respectively) as follows.

Eqn (7) in terms of $\tan\delta_1$, ω_1, E_c, τ_r, and E_r is as follows.

$$\tan\delta_1 = \frac{E_r\tau_r\omega_1}{E_c + (E_c + E_r)\tau_r^2\omega_1^2} \qquad (19)$$

Eqn (5) in terms of E_2', ω_2, E_c, τ_r, and E_r is as follows.

$$E_2' = \frac{E_c + (E_c + E_r)\tau_r^2\omega_2^2}{1 + \tau_r^2\omega_2^2} \qquad (20)$$

There are only two unknowns in the system given by eqn (19) and (20): E_r and τ_r, which can therefore be calculated by solving the system of equations. First, E_r can be expressed in terms of τ_r (as well as E_c, E_2', and ω_2) by rearranging eqn (20). Substituting the result (eqn (22)) into eqn (19) eliminates E_r and provides an expression for τ_r (eqn (21)). For ease of writing, E' of a GMM and SLS (formulas in Table S1, ESI†) is written as $E' = E_c + \chi$, where χ represents the contribution to E' from the N GMM arms (or single SLS arm) at a particular ω. The value of χ_2 is the difference between E_2' and E_c.

$$\left(\tan\delta_1 E_2'\omega_1^2\omega_2^2\right)\tau_r^3 - \left(\chi_2\omega_1\omega_2^2\right)\tau_r^2$$
$$+ \left(\tan\delta_1\left[E_c\omega_2^2 + \chi_2\omega_1^2\right]\right)\tau_r - \chi_2\omega_1 = 0 \qquad (21)$$

$$E_r = \chi_2\left(1 + \frac{1}{\tau_r^2\omega_2^2}\right) \qquad (22)$$

Note that, if the sample is a MW material, τ_r can be determined from the y-intercept of the model test line (eqn (13)) instead of eqn (21). Once τ_r and E_r are known, η can be calculated as $\eta = \tau_r E_r$. For materials obeying the SLS or GMM (not MW), τ_c can be calculated as $\tau_c = \eta/E_c$.

Since eqn (21) is a cubic polynomial, there are three possible values for τ_r. The root corresponding to the sample's τ_r can be determined by excluding negative and/or complex roots. If there is more than one real positive root, the root corresponding to the sample's τ_r can be selected by calculating $\tan\delta_1$ and E_2' from the material constants via the relevant equation (formulas in Table S1 (ESI†), use SLS formulas if the material is a GMM or SLS, or MW formulas if the material obeys the MW model) and choosing the value of τ_r which gives the closest calculated $\tan\delta_1$ and E_2' to the measured $\tan\delta_1$ and E_2'. If there are no real or positive roots, which can occur for numerical solvers if polynomials are flat in the root vicinity, alternate means of calculating sample parameters are described in Section S7 (ESI†).

2.3 Reconstructing frequency-dependent behavior

Once a sample's material constants are known, it is possible to calculate E', E'', and $\tan\delta$ of the material for a dynamic stimulus at any frequency by substituting the material constants into the relevant equation (Table S1, ESI†). Since GMM samples must be approximated as a SLS in order to calculate sample material constants, SLS equations should be used in the reconstruction for both SLS and GMM materials.

3 Analysis of error caused by performing bimodal AFM without tip radius calibration

For a spherical tip of radius R, E_2' is proportional to $\sqrt{1/R}$ (details in Section S4.1 and eqn (S14), ESI†).[18,28] Typically, R is estimated by measuring a calibration sample of known E_2', and manually altering R in the software until the measured E_2'

agrees with the known calibration E_2'.[19] The calibration sample should have similar E_2' to the actual sample.[19] However, selecting a calibration sample can be difficult for materials made of multiple components.

Without calibration, a less exact R can be obtained from the manufacturer's specifications for the tip, which include the mean tip radius $\bar{R}$ and range of possible radii. By definition of the standard deviation, the full range of R is larger than the standard deviation, S_R. However, equating S_R with the full range of possible radii provides a worst case estimate of the error caused by lack of R calibration.

The additional error in E_2' caused by taking R and S_R from the manufacturer specifications can be estimated from $\bar{R}$, S_R, the mean value of the measured E_2' $\left(\overline{E_{2,\mathrm{m}}'}\right)$, and the standard deviation of the measured E_2' $\left(S_{E_{2,\mathrm{m}}'}\right)$ via error propagation. The result is eqn (23), as derived in Section S5 (ESI†).

$$\frac{S_{E_2'}}{\left|\overline{E_2'}\right|} = \sqrt{\left(\frac{S_{E_{2,\mathrm{m}}'}}{\left|\overline{E_{2,\mathrm{m}}'}\right|}\right)^2 + \left(\frac{1}{2}\frac{S_R}{\left|\bar{R}\right|}\right)^2} \tag{23}$$

Therefore, the fraction of the error in E_2' due to uncertain R, written here as f_{ER}, is calculated as follows.

$$f_{\mathrm{ER}} = \sqrt{1 - \frac{S_{E_{2,\mathrm{m}}'}}{S_{E_2'}}} \tag{24}$$

Note that it is possible that R changes during an experiment due to tip blunting.[30] However, blunting can be discounted for two reasons. First, significantly blunt tips often prevent a repulsive tip/sample interaction.[30] As described in Section S4 (ESI†), calculation of $\tan\delta_1$ (eqn (S13), ESI†) requires a repulsive interaction, and the $\tan\delta_1$ map will be lost if this interaction is not repulsive.[26,27,30] Therefore, as long as a repulsive tip/sample interaction is maintained, it can be assumed that blunting is not significant enough to change $\bar{R}$ and S_R. Additionally, tips can become blunted during a measurement regardless of whether R is calibrated, so neglecting blunting in measurements with uncalibrated R does not introduce any additional error compared to calibrated R.

4 Validation of the novel analysis procedure

4.1 Materials and methods

A styrene–butadiene rubber (SBR) was used as a test sample for the new bimodal AFM analysis procedure due to the fact that SBRs are widely used, and therefore their properties are well known.[31] This particular SBR has already been characterized,[14,17] as published in Macromolecules.[17] Data from this characterization are reused here with permission from Macromolecules (see data permission at the end of the article for more details) to validate the new analysis procedure. The SBR is a GMM,[32] and possesses an adhesive tip/

sample contact.[14,17] These characteristics are ideal in testing how the new analysis procedure performs, because they are most likely to challenge bimodal AFM measurements. Specifically, the fact that the SBR obeys the GMM[32] will test whether a GMM can indeed be approximated as a SLS (as assumed in Section 2.1.1). Additionally, since calculation of E_2' uses the Hertz contact model and thereby assumes a non-adhesive contact,[18,28] the fact that the SBR has an adhesive tip/sample contact means that the measured E_2' is inaccurate.[6,17] If the new analysis procedure successfully works for the SBR in spite of these difficulties, the method is robust.

As detailed in the Macromolecules publication,[17] AFM experiments were performed on dry SBR samples with an Oxford Instruments Asylum Research Cypher ES AFM, using Oxford Instruments Asylum Research software version 16.9.220 in Igor Pro software version 6.38B01. AFM experiments were performed using AC240TSA cantilevers ($k_{\mathrm{c},1} \sim 2.5$ N m^{-1}, $k_{\mathrm{c},2} \sim 50$ N m^{-1}, $f_{\mathrm{c},1} \sim 60$ kHz in air, and $f_{\mathrm{c},2} \sim 390$ kHz in air, $R \sim 7 \pm 3$ nm) and AC160TSA cantilevers ($k_{\mathrm{c},1} \sim 13$ N m^{-1}, $k_{\mathrm{c},2} \sim 364$ N m^{-1}, $f_{\mathrm{c},1} \sim 290$ kHz in air, and $f_{\mathrm{c},2} \sim 1.5$ MHz in air, $R \sim 7 \pm 3$ nm), driven via photothermal actuation with full excitation laser (Oxford Instruments Asylum Research blueDrive™, 405 nm wavelength) power, and calibrated via Asylum Research's GetReal™ calibration method[30,33,34] in order to avoid blunting the tip.

Amplitude modulation–frequency modulation AFM (AM–FM AFM) was performed on the SBR. AM–FM AFM is a bimodal imaging technique that drives the AFM cantilever at two eigenmodes, measuring sample $\tan\delta_1$ via the lower frequency eigenmode undergoing amplitude modulation (AM)[26,27] and sample E_2' via the higher frequency eigenmode undergoing frequency modulation (FM).[18,19,25,28] The second mode is also subject to a dissipation feedback loop to prevent the second mode's oscillation from dropping beneath the detection limit.[19,25,28] Further details on AM–FM AFM can be found in note S4 (ESI†), and the formulas to calculate $\tan\delta_1$ and E_2' in Section S4.1 (ESI†).

Two AM–FM AFM experiments were performed. First, a single spot on the SBR was scanned multiple times with a variety of drive amplitudes and setpoints, to test if AM–FM AFM could provide stable quantification of E_2' and $\tan\delta_1$ without calibrating R. Second, multiple spots on the SBR were scanned to quantify the SBR's E_2' and $\tan\delta_1$. After the final spot on the SBR surface, nanoscale dynamic mechanical analysis (nDMA) was performed at select points in the final AM–FM AFM image. The second AM–FM AFM scan (over different spots on the sample), nDMA, and macroscale DMA (mDMA) of the SBR have already been published,[6,14,17] and are used here with permission to serve as controls for the output of the novel analysis procedure. Macroscale DMA details are provided in Section S2 (ESI†). Nanoscale DMA details can be found in Section S3 (ESI†).

For data processing, AM–FM AFM height images of SBR topography were flattened using Asylum Research software version 16.10.208 in Igor Pro software version 6.38B01, in order

to remove any variations in sample topography that were not due to SBR features. This flattening was done by hand, in order to avoid introducing flattening artifacts. The processed files were then analyzed by a custom script in MATLAB R2019b 9.7.0.1261785 that calculated $\tan\delta_1$ and E_2' of the sample (eqn (S13) and (S14), Section S4.1, ESI†), then applied the new bimodal AFM analysis procedure (Section 2). Results from the analysis procedure developed in this paper were compared to both nDMA and mDMA measurements.[14,17] The new bimodal AFM analysis procedure was considered valid if the calculated SBR parameters reproduced values similar to nDMA and mDMA measurements of the SBR.

4.2 SBR results

4.2.1 Distributions and statistics of SBR AM–FM AFM data. As shown in Fig. 1, individual AM–FM AFM maps/images of the SBR had varying distributions of E_2' and $\tan\delta_1$. Such variation likely arose from variation in the features, curvature, or topography, of the sample surface at any given area, since the shallow indentations in AM–FM AFM render AM–FM AFM measurements susceptible to sample topography.[19,27] Histograms of all pixel values in a single image of $\tan\delta_1$ or E_2' exhibited unimodal or bimodal distributions. As shown in Fig. 1(A), the presence of bimodal distributions in the data influenced calculation of the mean and standard deviation of AM–FM AFM measurements, and thereby resulted in values that did not accurately represent the data. To overcome this issue, the mean and standard deviation of AM–FM AFM measurements of the SBR were calculated by fitting Gaussians to the data distributions, as described in Section S8 (ESI†), rather than *via* the standard formulas. Fig. 1(A) shows that calculating

the mean from Gaussians results in statistics that represent the most prominent peak of the distribution. Fig. 1(B) shows that this Gaussian fit method of calculating sample statistics matches the values from the standard formulas if the data distribution is unimodal. For individual image statistics, the distribution used for the fit comprised of pixel values from a single AM–FM AFM image. For overall statistics, the distribution comprised of pixel values from all AM–FM AFM images of the SBR. Note that this method of calculating the mean and standard deviation was only necessary for E_2' and $\tan\delta_1$, and was not employed for other SBR parameters.

4.2.2 Measurement error due to uncalibrated tip radius. It was first necessary to ensure that lack of tip radius (R) calibration does not interfere with correct quantification of E_2' and $\tan\delta_1$. To this end, the effect of user controlled parameters during an AM–FM AFM experiment was studied by scanning a single spot on the SBR multiple times, with a variety of drive amplitudes and setpoints, in order to ensure that, regardless of how the user handled the AFM, the measured E_2' and $\tan\delta_1$ were consistent.

As detailed in Section S4 (ESI†), during an AM–FM AFM experiment, the user controls the amplitude feedback loops for both modes (AM for the first mode, and dissipation feedback for the second mode) by changing the setpoint, A_s, and drive amplitude of each mode.[19,25,30] Note that the user does not directly control FM of the second mode because the cantilever's resonance frequency is what regulates the FM feedback loop.[19,25,30] The drive amplitude determines the free amplitude, used as a reference amplitude, A_r, of the cantilever's oscillation.[30] Combinations of user-controlled parameters (A_s and A_r) can be summarized by a single metric for each eigenmode, the ratio of $A_{s,1}/A_{r,1}$ and $A_{s,2}/A_{r,2}$. The lower the ratio, the harder the user is tapping on the sample.[30]

To examine the feasibility of performing bimodal AFM without first calibrating R, AM–FM AFM was performed on the SBR with a variety of A_s/A_r combinations for each mode. This test was performed to ensure that: (i) AM–FM AFM could still correctly quantify a sample's E_2' even without first calibrating R, (ii) that uncertain R did not result in too large an error in E_2' (see Section 3), and (iii) test how $\tan\delta_1$ and E_2' depended on user-determined parameters. The test in (iii) is necessary to ensure that the values of $\tan\delta_1$ and E_2' are stable regardless of how the user handles the AFM during an experiment. If $\tan\delta_1$ and E_2' vary with A_s/A_r, it would be difficult to determine the actual value of the sample without calibrating R.

Fig. 2 shows the effect of A_s/A_r on the mean E_2' and $\tan\delta_1$. Results were similar for both cantilevers. The dissipation feedback parameters ($A_{s,2}/A_{r,2}$) did not affect $\tan\delta_1$ and E_2'. This result is expected, because the dissipation feedback of mode 2 prevents the mode's amplitude from falling below the detection floor, and is not used in AM–FM AFM calculations (Section S4).[19,25,28]

AM feedback parameters affected E_2' and $\tan\delta_1$. In general, if $A_{s,1}/A_{r,1}$ was too high, the value of $\tan\delta_1$ and E_2' varied more in response to changes in $A_{s,1}/A_{r,1}$. If $A_{s,1}/A_{r,1}$ was too low, the topography image became distorted or the dissipation feedback could no longer operate. In the later case, the dissipation
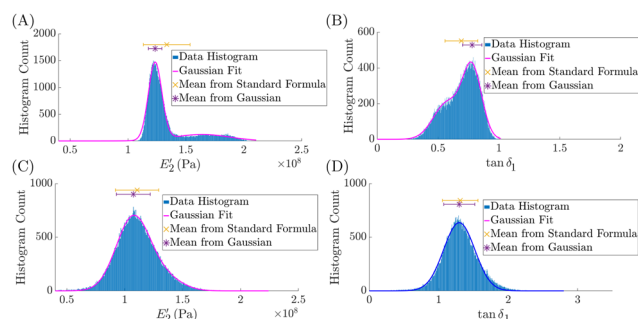

Fig. 1 Representative distributions of SBR AM–FM AFM measurements. All distributions were obtained from the values of individual pixels from a single AM–FM AFM image of the styrene–butadiene rubber sample (SBR). Two different AM–FM AFM images, collected on different areas of the SBR surface, are shown. Storage modulus, E_2', and loss tangent, $\tan\delta_1$, distributions from the first image are shown in (A) and (B), respectively, and from the second image are shown in (C) and (D), respectively. A Gaussian fit (see Section S8, ESI†) to the distribution is shown as a magenta line if a two term Gaussian was used or as a dark blue line if a single term Gaussian was used. The mean (points) and standard deviation (error bars) calculated *via* the standard formulas and *via* the Gaussian fit constants are shown as an orange × or a purple asterisks, respectively. These measurements were obtained with an AC240TSA cantilever, but are also representative of those obtained with an AC160TSA.
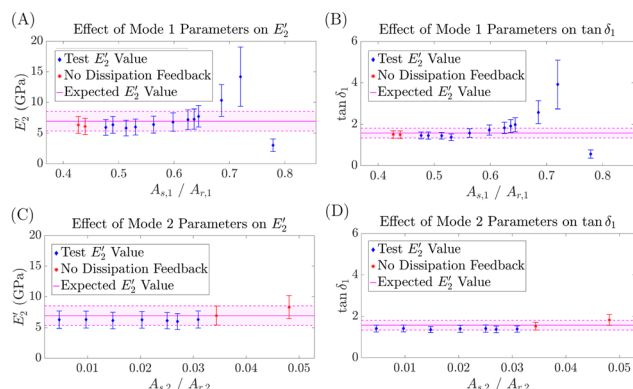
Fig. 2 Effect of user-controlled parameters on AM–FM AFM measure-ments. The ratio of setpoint A_s over free amplitude A_r of each AM–FM AFM eigenmode is controlled by the user. The effect of the lower frequency mode, mode 1, $A_{s,1}/A_{r,1}$ on E_2' and $\tan\delta_1$ is shown in (A) and (B), respectively (blue diamonds). The same for the higher frequency mode, mode 2, is shown in (C) and (D), respectively (blue diamonds). Red asterisks indicate images where the AFM could not adequately track dissipation of the second mode (due to the specific A_s and A_r), and thus could not adequately perform dissipation feedback. Magenta lines indicate the mean value of E_2' and $\tan\delta_1$ from AM–FM AFM data not part of the imaging parameter test. Error bars and shading represent the standard deviation of each measurement.

feedback was likely lost because the tip was tapping the sample too hard, interfering with the AFM's ability to drive the second mode. Regardless, loss of the dissipation image or distortion in the sample's features during the scan are signs that the user's $A_{s,1}/A_{r,1}$ is too high or too low to accurately quantify the sample. Still, AM–FM AFM quantification of $\tan\delta_1$ and E_2' was stable for several values of $A_{s,1}/A_{r,1}$. These results suggest that reliable and consistent quantification of $\tan\delta_1$ and E_2' can be obtained as long as the user decreases $A_{s,1}/A_{r,1}$ just enough to ensure a repulsive tip/sample interaction (where phase one obeys $\phi_1 < 90°$, to employ eqn (S13), ESI†) and a stable value of E_2' and $\tan\delta_1$. Representative AM–FM AFM images of the SBR obtained using this procedure are shown in Fig. 3.
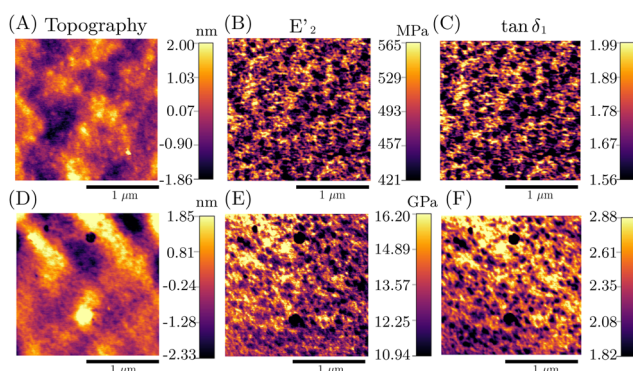

Fig. 3 Representative AM–FM AFM images of the SBR. SBR topography (A) and (D), storage modulus E_2' (B) and (E), and loss tangent $\tan\delta_1$ (C) and (F) are shown. Scale bars are 1 μm. The images in (A)–(C) were obtained using an AC240TSA cantilever, and are representative of the 25 AC240TSA images. Images in (D)–(F) were obtained using an AC160TSA cantilever, and are representative of the 13 AC160TSA images of the SBR.

After performing AM–FM AFM at multiple spots on the SBR surface, resulting in 25 AM–FM AFM images from AC240TSA scans and 13 images from AC160TSA scans, the mean E_2' and $\tan\delta_1$ were calculated by fitting a Gaussian to the resulting distributions for each quantity as described in Section 4.2.1. The mean $\pm$ standard deviation of the SBR's $\tan\delta_1$ was 1.9 $\pm$ 0.5 for the AC240TSA and 1.6 $\pm$ 0.4 for the AC160TSA. The mean $\pm$ standard deviation of the SBR's E_2' was 570 MPa $\pm$ 89 MPa for the AC240TSA and 7.0 GPa $\pm$ 0.6 GPa for the AC160TSA. Applying eqn (24), the uncertainty in R contributed to 79% of $S_{E_2'}$ from AC240TSA measurements and 65% of $S_{E_2'}$ from AC160TSA measurements. These results suggest that, if R is not calibrated, the uncertainty in R is not negligible, and should be propagated through the measured E_2'. However, E_2' can still be reliably measured, even without calibrating R. Note that one downside to lack of R calibration is that there is no longer an indication of tip/sample pairings where the Hertz contact model does not apply (e.g. adhesive contacts)[19] without the use of additional experiments like indentations, nDMA, or mDMA.

In order to ensure that AM–FM AFM measurements correctly quantified E_2' and $\tan\delta_1$, both quantities were compared with the nDMA and mDMA controls, and these results have already been published.[6,14,17] In summary, the measured $\tan\delta_1$ agreed well with the mDMA control.[6,14,17] However, AM–FM AFM's E_2' was 10–100× larger than E' measured by mDMA.[6,14,17]

Comparison of mDMA and AM–FM AFM data with nDMA measurements shows that the discrepancy between E_2' and the mDMA control is not due to uncertain R or the use of an incorrect $A_{s,1}/A_{r,1}$.[6,14,17] Instead, the observed overestimation of E_2' by AM–FM AFM is due to the fact that AM–FM AFM employs the Hertz contact model to calculate E_2',[18,28] since E' of nDMA calculated with the Hertz contact model shows similar disagreement with mDMA.[6,14,17] E' of nDMA calculated by modeling the contact geometry as a hyperboloid indenter with adhesion[14,17] agrees well with mDMA, suggesting that this model is the best contact model for the tip/SBR interaction.[6,14,17] In other words, adhesion is present between the tip and SBR. The Hertz contact model upon which AM–FM AFM relies assumes that no adhesion is present between the tip and sample,[5] and therefore inade-quately describes the tip/SBR interaction.[6,14,17] While reliance on the Hertz model results in an incorrect estimation of E_2' for AM–FM AFM, the value of $\tan\delta_1$ is correct because $\tan\delta$ is independent of contact geometry.[6,14,17,35]

In summary, quantification of $\tan\delta_1$ and E_2' in AM–FM AFM is still possible, even without using a sample of known modulus to calibrate R. Regardless of R calibration, incorrect quantifica-tion of E_2' will occur if the Hertz contact model is not suitable to describe the tip/sample interaction.

4.2.3 Determining the viscoelastic model to describe the SBR. Fig. 4 shows a representative plot of $y = \tan\delta_1^{-1}$ vs. $x = (E_2'\tan\delta_1)^{-1}$ (Section 2.1, eqn (12)) for AM–FM AFM data at a single spot on the SBR, that is, for a single AM–FM AFM image. Each image was fit with the model test line (eqn (12)). Fit

metrics for each image can be found in Table S2 (ESI†). The mean ± standard deviation R^2 value of the fits was 0.99 ± 0.02 for data measured with an AC240TSA, and 0.95 ± 0.04 for data measured with an AC160TSA. For both cantilevers, the slope and y-intercept of the fit were greater than zero (see Table S2, ESI†).

It is already known that the SBR is a GMM.[32] The good linear fit of the model test (eqn (12)) derived from SLS equations (Section 2.1) to SBR AM–FM AFM data suggests that a subgroup of GMM arms within the SBR, all with similar τ_n, contributed most to E_2' and $\tan\delta_1$. Specifically, the AM–FM AFM excitation frequencies in these experiments are more likely to excite GMM arms with τ_n on the order of 0.1–10 μs. The good fit of the SBR data to the model test line supports the notion that this subgroup of arms can be approximated as a single SLS, likely with a large standard deviation in its parameter values (E_c, E_r, and η), as discussed in Section 2.1.1.

While the model test plot in Fig. 4 can be fit with a line, the points seem to have a hyperbolic or logarithmic shape, rather than a linear shape. This observation suggests that the model test has a curve if the sample obeys the GMM, and a line if the sample obeys the SLS. It is reasonable to hypothesize that the curve in the model test line for a GMM may be due to superposition of all SLSs in the material that responded to the stimulus. Future investigation of this observation may improve the calculation of GMM material constants from AM–FM AFM data. Regardless, the large R^2 values of the linear fits suggest that, even though the model test appears to have a hyperbolic shape, a line still approximates the trend in the data well. Again, this observation supports the notion that bimodal AFM excites a subset of GMM arms, all with similar τ_n, and that can be approximated as a single SLS.

4.2.4 SBR material constants and frequency dependent behavior. SBR material constants, calculated *via* the new analysis procedure (Section 2.2), are shown in Table 1. As expected for a subgroup of GMM arms being approximated as a single SLS, the calculated material constants have large standard deviations. However, calculated material constants agree well with literature values.[31] Most of the parameter values agree between the SLS and the GMM. However, E_c is two orders of magnitude lower for the GMM than the SLS. Comparison with SBR DMA at low frequencies (Fig. 5(A)) shows that the GMM's
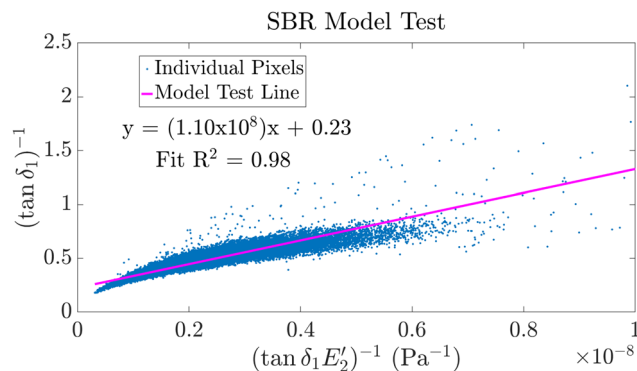

Fig. 4 Representative model test for a single AM–FM AFM image of the SBR. All pixels from a single AM–FM AFM image of the SBR are shown (points) along with the linear fit to the data (magenta line, eqn (12)), used to determine the best description of the SBR's viscoelastic response. The fit equation and R^2 value are also shown. The data in this figure are taken from a single AM–FM AFM image, but are representative of the fits to other images (fit details in Table S2, ESI†).

estimation of E_c is more accurate than the SLS's estimation. Therefore, to determine E_c of a GMM material, it is important to employ the calculation in Section 2.1.1, and not simply use that of the SLS (Section 2.1). Assuming that E_c is close to its upper bound (eqn (17) or (18)) calculated from the slope and y-intercept of the model test is still more accurate than taking E_c to be the slope of the model test (eqn (12)) if the sample obeys the GMM.

The values of SBR E', E'', and $\tan\delta$ over a range of frequencies ($E'(f)$, $E''(f)$, and $\tan\delta(f)$) were calculated by substituting the GMM material constants in Table 1, into eqn (5)–(7), respectively. This reconstruction of the SBR's frequency-dependent behavior is shown in Fig. 5 for AC240TSA cantilevers, and Fig. S2 (ESI†) for AC160TSA cantilevers. Reconstructions using SLS material constants are not shown, since GMM parameters (Table 1 and Section 2.1.1) are more accurate.

The accuracy of reconstructed $E'(f)$, $E''(f)$, and $\tan\delta(f)$ can be assessed *via* comparison to nDMA and mDMA control data (the control data has been previously published,[17] and is reused here with permission). Even though a hyperboloid indenter with adhesion is a better model of the tip/SBR interaction,[14,17] AM–FM AFM only uses the Hertz contact model to calculate E_2'.[18,28] Therefore, AM–FM AFM reconstructions should be

Table 1 Material constants of the SBR. Material constants were calculated for each AM–FM AFM image of different locations on the sample surface (a total of 25 for the AC240TSA and 13 for the AC160TSA). Table values represent the mean ± standard deviation of these calculations

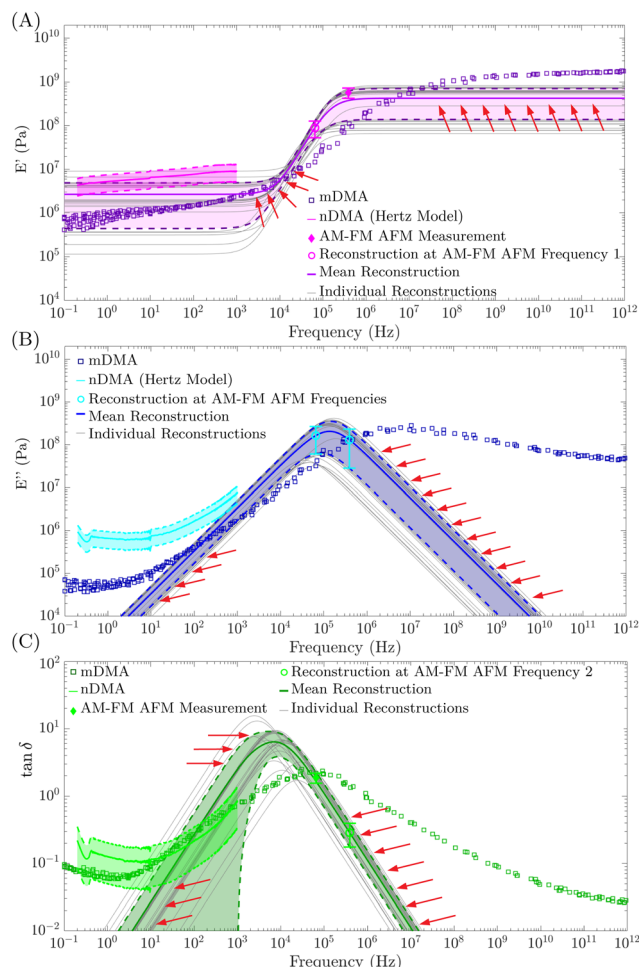| Parameter	Cantilever	GMM	SLS
E_c (Pa)	AC240TSA	$2.65 \times 10^6 \pm 2.27 \times 10^6$	$1.97 \times 10^8 \pm 1.26 \times 10^8$
	AC160TSA	$4.42 \times 10^7 \pm 1.07 \times 10^8$	$5.23 \times 10^9 \pm 1.00 \times 10^9$
E_r (Pa)	AC240TSA	$4.23 \times 10^8 \pm 2.86 \times 10^8$	$3.32 \times 10^8 \pm 2.61 \times 10^8$
	AC160TSA	$8.22 \times 10^9 \pm 1.50 \times 10^9$	$3.81 \times 10^9 \pm 1.70 \times 10^9$
η (Pa s)	AC240TSA	533.91 ± 257.52	406.57 ± 304.47
	AC160TSA	$2.82 \times 10^3 \pm 534.20$	$1.61 \times 10^3 \pm 636.79$
τ_r (s)	AC240TSA	$1.73 \times 10^{-6} \pm 0.97 \times 10^{-6}$	$1.34 \times 10^{-6} \pm 0.18 \times 10^{-6}$
	AC160TSA	$4.48 \times 10^{-5} \pm 8.08 \times 10^{-5}$	$2.34 \times 10^{-5} \pm 4.80 \times 10^{-5}$
τ_c (s)	AC240TSA	$3.45 \times 10^{-4} \pm 5.37 \times 10^{-4}$	$2.10 \times 10^{-4} \pm 1.85 \times 10^{-4}$
	AC160TSA	$3.44 \times 10^{-7} \pm 0.40 \times 10^{-7}$	$4.29 \times 10^{-7} \pm 0.32 \times 10^{-7}$

Fig. 5 Frequency dependent behavior of the SBR (AC240TSA). Storage moduli (E'), loss moduli (E''), and loss tangents ($\tan\delta$) over a range of frequencies are shown in (A)–(C), respectively. Mean AM–FM AFM reconstructions are compared to control macroscale dynamic mechanical analysis (mDMA, squares) and nanoscale DMA (nDMA, lines) measurements. All data besides the reconstructions have been published previously,[17] and are used here with permission. AM–FM AFM reconstructions from each of the 25 individual AM–FM AFM images are also shown in gray. Red arrows indicate regions where the reconstruction deviates from the controls by failing to account for all arms in the GMM. E' and E'' of nDMA measurements were calculated using the Hertz contact model. AM–FM AFM and nDMA were performed using an AC240TSA cantilever. Error bars and shading represent the standard deviation.

compared to nDMA data calculated with the Hertz contact model, not the adhesive hyperboloid model. In other words, AM–FM AFM reconstructions of $E'(f)$ and $E''(f)$ should match nDMA curves (Hertz model) at low frequencies, but should be 10–100× larger (Section 4.2.2) than mDMA values. The reconstructed $\tan\delta(f)$ should match both nDMA and mDMA data because $\tan\delta$ is independent of contact geometry.[14,17,35] At low frequencies, where $E' \sim E_c$ (see Section S1, Table S1, ESI†), the reconstruction aligns with the nDMA, suggesting that assuming E_c is close to the upper bound of E_c was correct for this sample. However, as previously described (Section 4.2.2), the estimated E_c, reconstruction E', and nDMA results are higher than mDMA values because the nanoscale measurements employ the Hertz contact model.

Red arrows in Fig. 5(A) indicate frequencies where the reconstruction of $E'(f)$ deviates from the controls. There are two main regions where the reconstruction does not accurately predict E'. First (i) is the transition between the low frequency and high frequency plateaus of E' (the glass transition of the SBR[36]), which occurs between 10^2–10^8 Hz in the mDMA. Second (ii) is the glassy plateau[8,36] of E' (at $f > 10^9$ Hz in the mDMA).

(i) For the glass transition,[8,36] mDMA shows that SBR E' transitions gradually (between 10^2–10^8 Hz) from the low frequency to the high frequency plateau. The transition in the reconstruction is sharper (ranges only between 10^4–10^6 Hz) and underestimates E' between 10^2–10^4 Hz. These observations suggest that the glass transition of the SBR results from a sum of the various contributions of multiple different τ_n of different orders of magnitude (*i.e.* ns, µs, ms, *etc.*...). This sum results in a broad glass transition, as expected for a GMM.[8] Since the AM–FM AFM reconstruction only uses a single τ_n, the transition is much sharper than the reality. Therefore, these results suggest that GMM arms in the subgroup that contribute to the SBR's response to AM–FM AFM stimulus are only part of the subgroup of arms that contributes to the SBR's glass transition.

(ii) For the glassy plateau[8,36] of the SBR (at $f > 10^9$ Hz), the reconstruction underestimates $E'(f)$. Again, this observation suggests that GMM arms that contribute most to this plateau are not part of the subgroup that dictates the SBR's response to AM–FM AFM stimulus. This observation is not surprising, since the microsecond τ_n that dictate the SBR's response to AM–FM AFM stimulus would respond too slowly to affect the SBR's response to higher frequency stimuli ($f > 10^7$ Hz).

As shown in Fig. 5(B), the reconstructed $E''(f)$ aligns well with nDMA results between 10^3–10^6 Hz. As expected, the value of E'' calculated by nDMA and the reconstruction is higher than that of mDMA due to the use of the Hertz contact model (as already discussed Section 4.2.2). For frequencies outside of this 10^3–10^6 Hz range, E'' is underestimated by the reconstruction (indicated by red arrows in Fig. 5(B)). This observation is a byproduct of using the SLS to approximate the GMM for the reconstruction. For the SLS, $N = 1$, and E'' increases to a peak at frequencies near the glass transition of the sample, then decreases again (eqn (6)). For a GMM, E'' can have a broader peak due to contributions from the additional τ_n.[8] Therefore, it is not surprising that $E''(f)$ is not adequately reconstructed for frequencies too slow or too fast for the subgroup of GMM arms that respond to AM–FM AFM stimulus.

In general, the reconstructed $\tan\delta(f)$ agrees with the nDMA and mDMA controls where $E'(f)$ and $E''(f)$ also agree with the controls, and deviates from nDMA and mDMA results when the reconstructed E' and E'' do so as well (Fig. 5(C)). Specifically, reconstructed $\tan\delta$ matches the controls well between 10^2–10^3 Hz, and again between 10^4–10^6 Hz. The lack of agreement between the reconstructed $\tan\delta$ and controls at 10^3–10^4 Hz is due to the reconstruction's inability to capture the glass transition between the low and high frequency plateaus in E'. The discrepancies between reconstruction $\tan\delta(f)$ and the controls at frequencies larger than 10^6 Hz, or smaller than 10^2 Hz are due to the reconstruction's inability to accurately model $E''(f)$.

Reconstructions performed with an AC160TSA (Fig. S2, ESI†) showed similar results. However, estimation of the transition in E' was more accurate, and therefore the reconstructed $\tan\delta$ was more accurate (although not an exact match to the controls) between 10^5 and 10^6 Hz. Additionally, reconstructed E_c was higher than that of the AC240TSA. This observation suggests that the accuracy of the reconstruction may vary, depending on where f_1 and f_2 occur relative to the glass transition of a sample. Based on mDMA, the SBR's glass transition was between 10^4 and 10^6 Hz. For the AC240TSA, f_1 and f_2 were roughly in the middle of this transition. For the AC160TSA, f_1 and f_2 occurred toward the higher frequency end of the transition. These results suggest that the reconstruction may be better at predicting lower frequency behaviors of a sample when f_1 and f_2 are lower than or inside the glass transition. If f_1 and f_2 are higher than the glass transition, the reconstruction may be better at predicting glass transition and high frequency behavior. These differences likely stem from assuming that E_c is approximately its upper bound (eqn (17) or (18)). Since f_1 and f_2 are higher for the AC160TSA, and measure values closer to the SBR's glassy plateau, the upper bound of E_c is calculated to be higher. In the future, it would be interesting to further test this hypothesis with additional cantilevers that have f_1 and f_2 at different frequencies relative to the glass transition of the sample.

Together, these results suggest that bimodal AFM data can be used to perform limited reconstructions of a GMM sample's frequency dependent $E'(f)$, $E''(f)$, and $\tan\delta(f)$. For the most-accurate measurement of a sample's frequency dependent behavior, it is best to combine bimodal AFM data with other techniques like nDMA, rather than rely only on the reconstruction of $E'(f)$ and $E''(f)$ from bimodal AFM data. However, bimodal AFM reconstructions can capture important quantities of a sample's frequency dependent behavior, especially for frequencies near f_1 and f_2. At the bare minimum, the reconstruction allows for fairly-accurate estimation of E' at f_1, E'' of at least one of the two measurement frequencies, and can be used to predict E_c of a sample. The method described here can still be used to approximate E_c of a GMM, as long as it is acknowledged that the value of E_c of a GMM is the upper bound, and not necessarily the exact value of E_c. To improve reconstruction accuracy, bimodal AFM measurements of the same sample with different cantilevers could be combined, for example by comparing E_2' and $\tan\delta_1$ between cantilevers. However, such reconstruction is beyond the scope of this work. The analysis procedure presented here can be employed even if only one cantilever is used to measure the sample. Additionally, for bimodal AFM measurements of samples that obey the GMM, it would be interesting to derive a method of estimating N from bimodal AFM data, possibly by comparing observations made with several cantilevers with different f_1 and f_2.

5 Discussion

The SBR selected to validate procedure outputs was well characterized,[17] but also likely to confound bimodal AFM

measurements *via* the non-Hertzian tip/sample contact,[17] and test the limits of the analysis procedure by adhering to the GMM[32] (Section 4.1). In spite of these complications, the procedure still yielded useful information about the sample's viscoelastic behavior. Additionally, the steps used in this article to assess procedure outputs are among several that can be employed to cross-validate procedure outputs for any sample. The following discussion describes potential means of improving bimodal measurements of samples like the SBR and how to cross-validate analysis procedure outputs for any sample measured by bimodal AFM.

The main confounding property of the SBR sample in this article was the adhesive, non-Hertzian tip/sample contact, meaning that bimodal AFM's use of the Hertz contact model to calculate E_2',[14,17] and therefore analysis procedure calculations of sample elastic constants and E'', yielded artificially high values compared to the mDMA control. To improve measurement accuracy, it is either necessary to apply additional contact models to bimodal AFM or place the sample in conditions that render the tip/sample contact Hertzian. The first, and most versatile, means of addressing the tip/sample contact would be to derive expressions to calculate E_2' in bimodal AFM measurements using other contact models besides the Hertz model. Currently, E_2' can also be calculated using the Lennard-Jones force (LJF) and Derjaguin–Muller–Toporov (DMT) contact models.[28] However, bimodal AFM theory could be expanded to include other contact models like the Johnson–Kendall–Roberts (JKR) model or the adhesive hyperboloid.

A second means to potentially eliminate non-Hertzian contacts on samples in air is to perform measurements in liquid instead. Liquid environments can reduce adhesive forces[37,38] and therefore increase the likelihood that the Hertz model applies. While liquid environments can reduce adhesive forces,[37,38] the mechanical properties of a sample often differ between air and liquid environments.[1] Therefore, control measurements such as mDMA or nDMA should be performed in similar conditions to bimodal measurements. It is also important to note that measuring a sample in liquid does not guarantee a Hertzian, or even a nonadhesive contact. For example, many biological samples still exhibit adhesion, even in liquid environments.[16]

Regardless of whether a non-Hertzian tip/sample contact can be addressed, the measurements in this paper demonstrate that the new analysis procedure can still be applied even if the Hertz model does not accurately describe the tip/sample interaction. At minimum, the procedure can help the user determine how best to model the sample's viscoelastic behavior. To assess the reliability of procedure outputs for a given sample, procedure outputs should be compared against other measurements, as in this article. Such cross-validation can be accomplished in several ways, depending on the control data available for comparison. Measurements that can be used to cross-validate analysis procedure outputs include: mDMA, nDMA, nanoindentation, relaxation experiments, creep experiments, and literature measurements of similar samples. The pros and cons of each cross-validation measurement, and how cross-

validation can be performed with each measurement, are elaborated in Section S9 (ESI†).

At minimum, it is important to cross-validate E_c of a GMM material. As described in Section 2.2, E_c is calculated first, then used to solve for the remaining material constants (eqn (21) and (22), Section 2.2). Additionally, if the sample is a GMM, it is necessary to assume that E_c is close to the bound on E_c (Section 2.1.1 and Section S6, ESI†). If this assumption does not apply, the estimation of E_c, and therefore all other parameters, will not be accurate. Therefore, it is essential to cross-validate E_c (see Section S9, ESI†) for any GMM sample. If procedure E_c does not match that of the cross-validation experiment, GMM parameter estimation should not be employed because the assumption necessary for the procedure to estimate E_c does not hold.

5.1 Likelihood of encountering a special case of the GMM

Note that it is difficult to find samples guaranteed to behave as one of the GMM's special cases, since the behavior of a sample is affected by experimental conditions. For example, collagen has been modeled with either the GMM or SLS, depending on experimental conditions.[9,39–44] While there is no guarantee that a sample will behave as a MW, KV, or SLS material, knowledge of each model's characteristics can help identify candidate samples more likely to obey the GMM's special cases.

In general, MW materials tend to be more fluid.[36] Therefore, samples with little crosslinking, weak iterations between constituent polymers, or made of mobile constituents would be more likely to obey the MW model. KV materials are more difficult to identify than MW materials. However, since $\tau_r = 0$ for a KV material, samples that do not exhibit relaxation are more likely to behave as a KV material. Relaxation experiments[16] could help identify candidate samples that do not relax. Finally, the SLS will apply in conditions that restrict the number of arms in a GMM that respond to bimodal stimulus. Such conditions might include thin and uniform samples, since there are fewer unique constituents in uniform samples, and fewer dimensions for polymers in the material to interact in thin samples, thereby reducing the number of arms in the GMM.

6 Conclusions

In summary, bimodal AFM techniques such as AM–FM AFM can be performed on samples to quantify $\tan\delta_1$ and E_2' of the sample, even without first calibrating the AFM tip radius on a sample of known modulus. If tip radius is not calibrated, the additional uncertainty in E_2' should be taken into account by propagating the uncertainty in R through measurements of E_2' (eqn (23)). Additionally, without tip radius calibration, there may be no indicator if the Hertz contact model does not apply unless bimodal AFM is performed together with other types of experiments such as nDMA, nanoscale indentations, or mDMA. Regardless of tip calibration or lack thereof, the measured E_2' can be incorrect if the Hertz contact model, on which bimodal AFM calculation of E_2' relies,[18,28] is not a good model for the tip/sample interaction. In the future, it would be prudent to expand (as already done for the DMT model and the Lennard-Jones potential *via* fractional calculus[28]) the calculation of E_2' in bimodal AFM to include other contact models like the Johnson–Kendall–Roberts model[5] and the adhesive hyperboloid.[14,17,45]

The new analysis procedure developed in this article (Section 2) can be used on bimodal AFM data to extract additional information about a sample's viscoelastic response. A flow chart of the procedure is shown in Fig. 6. First, $\tan\delta_1$ and E_2' can be used to test whether the sample obeys any of the standard models of linear viscoelasticity (MW, KV, SLS, and GMM), and distinguish between each model (Section 2.1, eqn (12)). Ability of the model test to distinguish different sample components that potentially obey different models of viscoelasticity was not assessed in this article. However, if material components do not all fall in the same group of points for the model test, it may be possible to use the model test to identify viscoelasticity of multiple components within a sample.

Once the best model for a sample's viscoelastic response is known, model parameters can then be calculated (Section 2.2), and the frequency dependent behavior of a sample's $E'(f)$, $E''(f)$, and $\tan\delta(f)$ can be reconstructed (Section 2.3). Accuracy of the reconstruction is limited if the sample is a GMM, and depends on where the measurement frequencies fall in the sample's rheological behavior (for example, relative to the glass transition), but can at minimum, provide the value of E_1', a bound for E_c, and E'' of at least one of the two measurement frequencies. For the most accurate measurement of $E'(f)$, $E''(f)$, and $\tan\delta(f)$, it is best to combine bimodal AFM with other techniques like nDMA, rather than rely solely on the reconstruction. Regardless, future bimodal AFM experiments can use the analysis procedure developed in this article to gain additional insight into a sample's viscoelastic behavior, especially which model of linear viscoelasticity best applies to the sample, and thereby gain additional insight into a sample's function or application.

Author contributions

C. E. A. conceptualized and designed the new bimodal AFM analysis procedure. C. E. A. performed AM–FM AFM measurements and reconstructions of the SBR, and carried out data visualization. C. E. A. and A. R. P. discussed validation of the new analysis procedure and SBR data interpretation. A. R. P., C. E. A., and S. C. are authors on the previously-published SBR data. C. E. A and S. C. wrote the article with feedback from all other authors. S. W. and S. C. supervised the work.

Data availability

Several of the SBR measurements, specifically the mean and standard deviation of SBR AM–FM AFM measurements (displayed as lines in Fig. 2 and filled points in Fig. 5 and Fig. S2, ESI†), nDMA measurements (displayed in Fig. 5 and Fig. S2, ESI†), and mDMA measurements (displayed in Fig. 5 and Fig. S2, ESI†) in this paper have previously been published in Macromolecules,[17] and are used here with permission. The
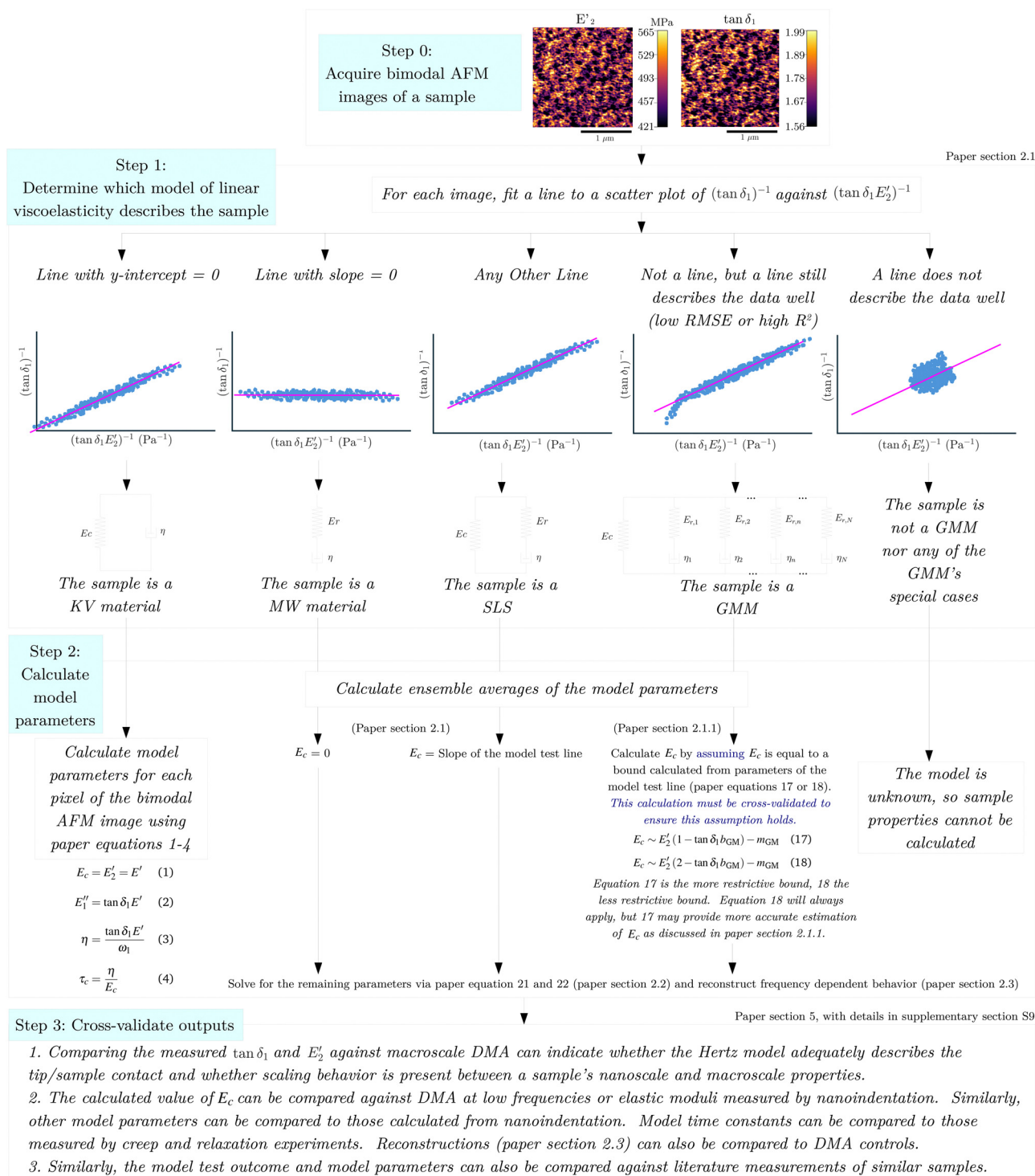
Fig. 6 Procedure flow chart.

Macromolecules publication can be found at **https://pubs.acs.org/doi/10.1021/acs.macromol.3c02052** or **https://doi.org/10.1021/acs.macromol.3c02052**.

Conflicts of interest

There are no conflicts of interest to declare.

Acknowledgements

Notes and references

1 M. Doi, *Soft matter physics*, Oxford University Press, 1st edn, 2013.

2 R. S. Lakes, *Rev. Sci. Instrum.*, 2004, **75**, 797–810.

3 U. S. Schwarz and S. A. Safran, *Rev. Mod. Phys.*, 2013, **85**, 1327–1381.

4 J. Seifert, *In vivo dynamic AFM mapping of viscoelastic properties of the primary plant cell wall*, 2018.

5 V. L. Popov, M. Heß and E. Willert, *Handbook of Contact Mechanics: Exact Solutions of Axisymmetric Contact Problems*, Springer Berlin Heidelberg, 2019.

6 C. Adam, *Physical Regulation of Cell Behaviors: Multifrequency AFM Measurement of Mechanoelectric, Mechanochemical, and Hydration Shell Effects on ECM and Cell Substrate Viscoelasticity*, 2021.

7 L. E. Nielsen, *Mechanical properties of polymers and composites*, M. Dekker, New York, 1974.

8 J. D. Ferry, *Viscoelastic properties of polymers*, Wiley, 3rd edn, 1980.

9 B. Xu, H. Li and Y. Zhang, *Biomatter*, 2013, **3**, e24651.

10 R. Y. Dhume and V. H. Barocas, *Acta Biomater.*, 2019, **87**, 245–255.

11 J. Honerkamp and J. Weese, *Macromolecules*, 1989, **22**, 4372–4377.

12 N. Orbey and J. M. Dealy, *J. Rheol.*, 1991, **35**, 1035–1049.

13 S. L. Hansen, P. M. Ray, A. O. Karlsson, B. Jørgensen, B. Borkhardt, B. L. Petersen and P. Ulvskov, *Plant Physiol.*, 2011, **155**, 246–258.

14 A. R. Piacenti, *Atomic Force Microscope-Based Methods for the Nano-Mechanical Characterisation of Hydrogels and other Viscoelastic Polymeric Materials for Biomedical Applications*, 2021.

15 H.-J. Butt, B. Cappella and M. Kappl, *Surf. Sci. Rep.*, 2005, **59**, 1–152.

16 Y. M. Efremov, T. Okajima and A. Raman, *Soft Matter*, 2020, **16**, 64–81.

17 A. R. Piacenti, C. Adam, N. Hawkins, R. Wagner, J. Seifert, Y. Taniguchi, R. Proksch and S. Contera, *Macromolecules*, 2024, **57**, 1118–1127.

18 A. Labuda, M. Kocuń, W. Meinhold, D. Walters and R. Proksch, *Beilstein J. Nanotechnol.*, 2016, **7**, 970–982.

19 M. Kocun, A. Labuda, W. Meinhold, I. Revenko and R. Proksch, *ACS Nano*, 2017, **11**, 10097–10105.

20 S. D. Solares and G. Chawla, *Meas. Sci. Technol.*, 2010, **21**, 125502.

21 G. Haugstad, *Atomic force microscopy: understanding basic modes and advanced applications*, John Wiley & Sons, 2012.

22 R. García, *Surf. Sci. Rep.*, 2002, **47**, 197–301.

23 R. Castro García, *Amplitude modulation atomic force microscopy*, 2011.

24 Z. Al-Rekabi and S. Contera, *Proc. Natl. Acad. Sci. U. S. A.*, 2018, **115**, 2658–2663.

25 S. Benaglia, V. G. Gisbert, A. P. Perrino, C. A. Amo and R. Garcia, *Nat. Protoc.*, 2018, **13**, 2890–2907.

26 R. Proksch and D. G. Yablon, *Appl. Phys. Lett.*, 2012, **100**, 073106.

27 R. Proksch, M. Kocun, D. Hurley, M. Viani, A. Labuda, W. Meinhold and J. Bemis, *J. Appl. Phys.*, 2016, **119**, 134901.

28 E. T. Herruzo and R. Garcia, *Beilstein J. Nanotechnol.*, 2012, **3**, 198–206.

29 J. Seifert, C. Kirchhelle, I. Moore and S. Contera, *Acta Biomater.*, 2021, **121**, 371–382.

30 *Applications Guide Version 16 Revision*, Oxford Instruments Asylum Research Manual, 2018.

31 M. H. Harandi, F. Alimoradi, G. Rowshan, M. Faghihi, M. Keivani and M. Abadyan, *Results Phys.*, 2017, **7**, 338–344.

32 R. Esmaeeli and S. Farhad, *Mech. Mater.*, 2020, **146**, 103369.

33 M. J. Higgins, R. Proksch, J. E. Sader, M. Polcik, S. Mc Endoo, J. P. Cleveland and S. P. Jarvis, *Rev. Sci. Instrum.*, 2006, **77**, 013701.

34 *Get Real – Automated Probe Calibration*, Oxford Instruments Asylum Research Forums, **https://support.asylumresearch.com/articles/video-tutorials-aa/19721-getreal-automated-probe-calibration**, 2014.

35 K. Menard, *Dynamic Mechanical Analysis: A Practical Introduction*, CRC Press, 2nd edn, 2008.

36 D. Roylance, *Engineering Viscoelasticity*, Massachusetts Institute of Technology, **https://web.mit.edu/course/3/3.11/www/modules/visco.pdf**, 2001.

37 A. L. Weisenhorn, P. K. Hansma, T. Albrecht and C. F. Quate, *Appl. Phys. Lett.*, 1989, **54**, 2651–2653.

38 *Encyclopedia of Nanotechnology*, ed. B. Bhushan, Springer, 2012.

39 E. J. Amis, C. J. Carriere, J. D. Ferry and A. Veis, *Int. J. Biol. Macromol.*, 1985, **7**, 130–134.

40 S. Meghezi, F. Couet, P. Chevallier and D. Mantovani, *Int. J. Biomater.*, 2012, 1–9.

41 S. Nam, K. H. Hu, M. J. Butte and O. Chaudhuri, *Proc. Natl. Acad. Sci. U. S. A.*, 2016, **113**, 5492–5497.

42 N. Sasaki, in *Viscoelasticity – From Theory to Biological Applications*, ed. J. De Vicente, InTech, 2012.

43 Z. Shen, H. Kahn, R. Ballarini and S. Eppell, *Biophys. J.*, 2011, **100**, 3008–3015.

44 R. Sopakayang, R. De Vita, A. Kwansa and J. W. Freeman, *J. Theor. Biol.*, 2012, **293**, 197–205.

45 Y. Sun, B. Akhremitchev and G. C. Walker, *Langmuir*, 2004, **20**, 5837–5845.